Transition Metal-Oxide Nanomembranes Assembly by Direct Heteroepitaxial Growth

Li, Hang; Yun, Shinhee; Chikina, Alla; Rosendal, Victor; Tran, Thomas; Brand, Eric; Christoffersen, Christina H.; Plumb, Nicholas C.; Shi, Ming; Pryds, Nini

Total number of authors:
11

Published in:
Advanced Functional Materials

Link to article, DOI:
10.1002/adfm.202313236

Publication date:
2024

Document Version
Version created as part of publication process; publisher's layout; not normally made publicly available

ADVANCED FUNCTIONAL MATERIALS
www.afm-journal.de

Transition Metal-Oxide Nanomembranes Assembly by Direct Heteroepitaxial Growth

Hang Li, Shinhee Yun, Alla Chikina, Victor Rosendal, Thomas Tran, Eric Brand, Christina H. Christoffersen, Nicholas C. Plumb, Ming Shi, Nini Pryds,* and Milan Radovic**

The integration of complex oxides with a wide range of functionalities on conventional semiconductor platforms is highly demanded for functional applications. Despite continuous efforts to integrate complex oxides on Si, it is still challenging to harvest epitaxial layers using standard deposition processes. Here, a novel method is demonstrated to create high-quality complex heterostructures on Si integrated with $SrTiO_3$ membranes as a universal platform. The STO membrane successfully bridges a broad spectrum of complex heterostructures such as $SrNbO_3$, $SrVO_3$, TiO_2, and dichalcogenide 2D superconducting FeSe toward semiconducting wafers (Si). Through electronic structures measured by angle-resolved photoemission spectroscopy, the high quality and functionality of the heterostructures are verified. This study demonstrated a new pathway toward realizing electronic devices with multifunctional physical properties incorporated into Si.

1. Introduction

Advancing from macro-scale 3D materials to nanoscale quasi-2D thin films holds significant promise in enabling intriguing properties for modern devices. Currently, two prevailing methods for synthesizing crystalline 2D materials are available: (1) hetero-epitaxy on a given substrate and (2) mechanical exfoliation. Strain induced by different lattice parameters in hetero-epitaxy or constructed hetero-interface may offer an additional degree of freedom for tailoring emerging phenomena.[1–7] Exfoliation[8] on the other hand, is recognized as a universal way to prepare artificial 2D materials heterostructures.[9] Recently, three strategies for fabricating freestanding transition metal-oxide (TMO) membranes were developed: (1) free-standing membranes using water-soluble sacrificial crystal layers,[10–14] (2) remote epitaxy,[15,16] and (3) self-formed free-standing membrane.[17] Artificial heterostructures were also fabricated by stacking and twisting membranes directly.[18] These results demonstrate an exciting approach for producing freestanding membranes and stacks, e.g., made of perovskite oxides, one of the largest oxide families with a broad range of important physical and chemical properties and transferring these onto any substrate thus bypassing the epitaxial roadblock. Here, Strontium Titanate ($SrTiO_3$, STO) represents a vital perovskite-type substrate due to its exceptional properties.

Since the growth of the first STO crystal by Leon Merker,[19] it has exhibited excellent properties such as dielectric,[20] ferroelectric,[21–25] piezoelectric,[26] and superconducting,[27,28] making it a suitable candidate for various technological applications. The lattice parameter of STO closely matches with many important perovskite oxides and other functional materials, which is crucial for minimizing defects and strain in the epitaxial films under oxygen-rich environment, leading to improved device performance and reliability. This makes STO the most commonly used substrate for the growth of perovskite-type TMO thin films and heterostructures.

A key prerequisite for the practical application of functional oxides is the ability to grow perovskite (here STO) thin films directly on Si. As an alternative to SiO_2, TMO-Si system acts as a more functional platform exceeding the traditional Si—SiO_2 field effect transistor.[22] It is non-trivial to grow STO on Si[22,29] since conventional growth procedures on a Si substrate result in polycrystalline, amorphous, or single crystalline depending on the growth conditions. Monolithic integration of STO membranes (STOm) on the Si platform has been proposed as an alternative approach.[10–16] Using this procedure, it is possible to transfer millimetre-size single-crystalline of STOm onto Si (STOm-Si), with good adherence between the transferred oxide membrane and the Si template.[10–16] Indeed, this approach provides a template allowing heterogeneous integration of TMO materials with appealing properties on semiconducting wafers.

H. Li, A. Chikina, N. C. Plumb, M. Shi, M. Radovic
Photon Science Division
Paul Scherrer Institute
Villigen 5232, Switzerland
E-mail: hang.li@psi.ch; milan.radovic@psi.ch

S. Yun, V. Rosendal, T. Tran, E. Brand, C. H. Christoffersen, N. Pryds
Department of Energy Conversion and Storage
Technical University of Denmark
Kongens Lyngby 2800, Denmark
E-mail: nipr@dtu.dk

The ORCID identification number(s) for the author(s) of this article can be found under https://doi.org/10.1002/adfm.202313236

DOI: 10.1002/adfm.202313236

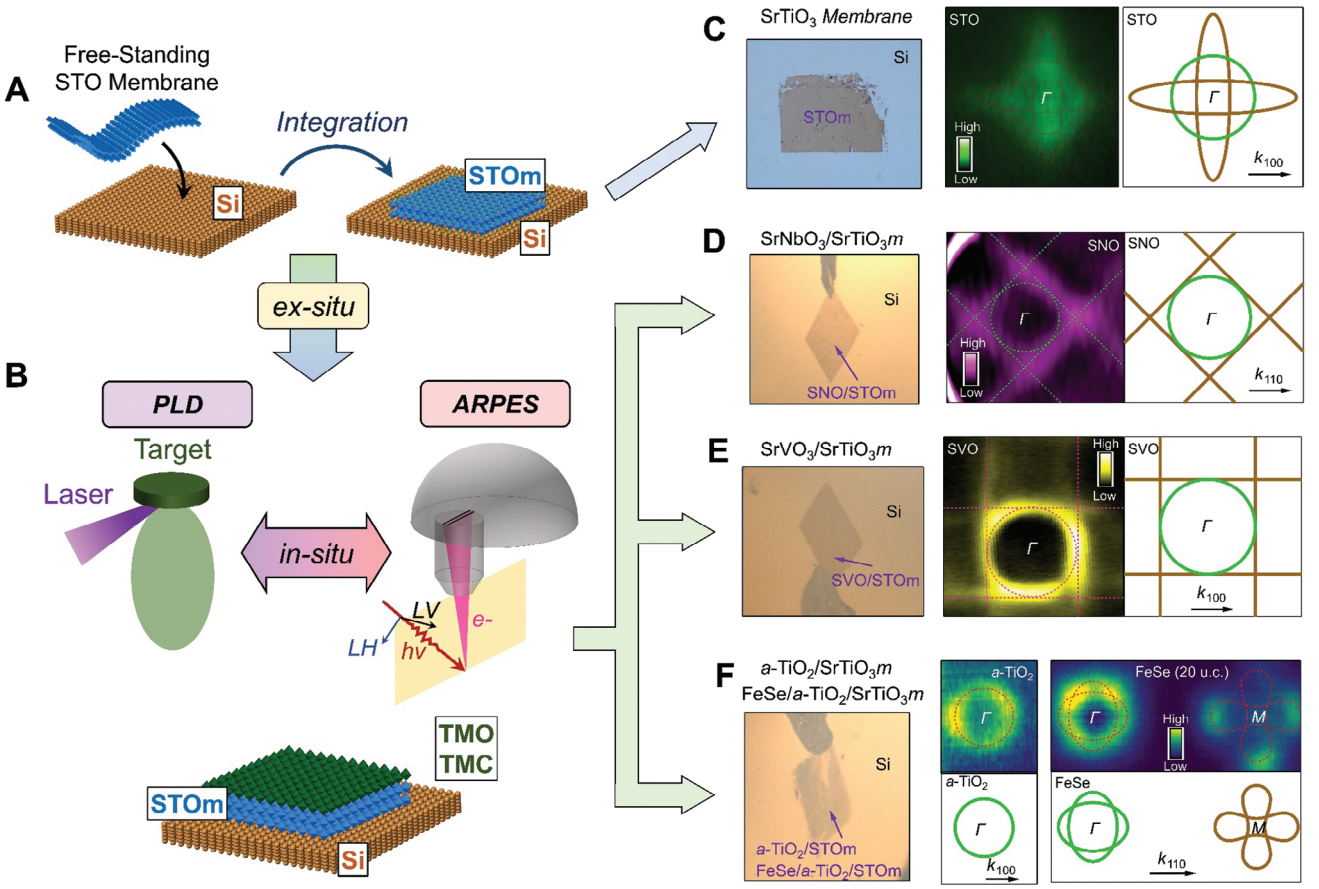

Figure 1. The schematic view of the research. A) Integration of free-standing STOm to Si wafer. B) Hetero-epitaxial growth of functioning materials, transition metal-oxides (TMO) and transition metal chalcogenide (TMC) on Si-integrated STOm and in-situ ARPES measurements. C-F) left: photograph of STOm and hetero-epitaxial films on STOm. Right: 2D curvature FS maps measured by ARPES with guide of FSs plotted upon and schematics of FS topography, respectively.

Here, we introduce an innovative method for crafting and transferring high-quality freestanding STOm. We seamlessly integrate these membranes onto Si substrates (as shown in **Figure** 1A) and proceed to deposit a diverse array of epitaxial complex oxides atop the STOm-Si templates (refer to Figure 1B). This method allows us to:

Circumvent the challenges associated with certain TMOs that undergo notable chemical alterations when exposed to water. Such reactions pose difficulties in releasing and transferring these freestanding layers. Our solution is to deposit the epitaxial layer directly in a vacuum chamber onto the STOm-Si template. This eliminates the risk of the complex oxide being in direct contact with water or other chemicals necessary to dissolve sacrificial crystal layers.

Establish a universal Si template that incorporates a standalone STOm. The quality of this template rivals that of its single-crystal counterparts and surpasses that of thin films. This means that any labs can utilize the deposition directly on STO, eliminating the need for additional layer releases or transfers for subsequent film growth.

We have demonstrated epitaxial growth and functionality by examining the electronic structures of materials such as $SrNbO_3$ (SNO), $SrVO_3$ (SVO), anatase TiO_2 (*a*-TiO2), and FeSe thin films/heterostructures (illustrated in Figure 1B). All the layers and heterostructures which were characterized showed impeccable quality. In fact, when analyzed using angle-resolved photoemission spectroscopy (ARPES), their electronic structures were found to be on par with, their single crystalline versions (as depicted in Figure 1C-F). In essence, our breakthrough paves the way for integrating oxide heterostructures with Si-based semiconductor device designs. We detail the process of epitaxially growing a broad spectrum of complex-oxide materials on the STOm-Si templates in the following sections.

2. Freestanding STO Membranes Templets

Freestanding STOm with thicknesses of 10 and 30 nm were fabricated by epitaxial growth on single-crystal (001)-oriented STO substrate with a buffered water-soluble 10 nm-thick SAO sacrificial layer using PLD.[14] The quality of the grown STO films on the SAO sacrificial layer is elucidated by the appearance of step terraces as feature by atomic force microscopy (AFM) (**Figure** 2A_i,B_i). The STOm were then exfoliated by dissolving the SAO layer in de-ionized water and transferring these onto the Si wafer (See Method Section and Figure 1A). Millimeter size STOm were transferred with minimum microcracks and

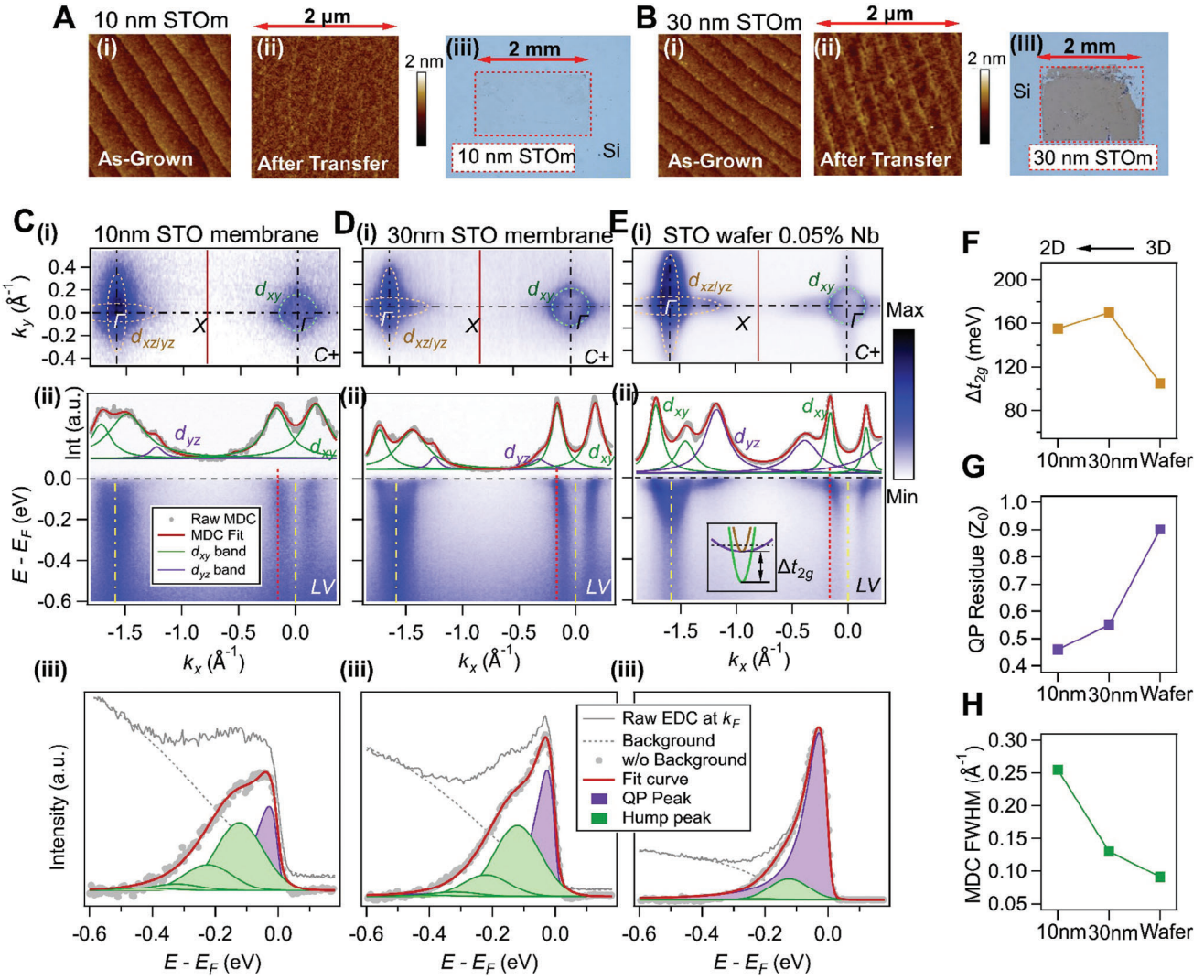

Figure 2. Electronic structures of STOm and STOw. A) Atomic force microscopic images of as-grown 10 nm thick STOm (i) and after transfer and annealed on Si (ii). (iii) The microscopic photograph of STOm after transfer. The flake marked by red dashed squares indicates the membranes with the size ≈1 × 2 mm^2. B) same as A but for 30 nm thick STOm. C) (i), in-plane Fermi surface maps of STOm with thickness of 10 nm, (ii) ARPES intensity cuts along Gamma-X direction of STOm 10 nm. The black dashed lines mark the Fermi energy, and the yellow dashed-dot lines mark the high symmetry points. The grey dots indicate the momentum distribution curves (MDCs) at E_F. The green and purple fitted Lorentzian peaks indicate the d_{xy} and d_{yz} bands, respectively. (iii) energy distribution curves (EDCs) extracted at the k_F of d_{xy} bands (red dashed lines) in (ii), respectively. Figure annotations are shown in E_{iii}. The QP and hump structures are fitted by Franck-Condon model. D and E) same as C but for 30 nm thick STOm and STO wafer, respectively. F) Δt_{2g} (illustrated in E_{ii}) of 10/30 nm STOm and STOw. The extraction details are shown in Figure S3 (Supporting Information). G) fitted quasiparticle residue (Z_0) from the EDCs in C_{iii}-E_{iii}. H) FWHM of fitted d_{xy} Lorentzian peaks by the momentum distribution curves (MDC) at E_F in C_{ii}-E_{ii}.

wrinkles (Figure 2A$_{iii}$,B$_{iii}$). Post-annealing process was performed after the transfer in order to remove contamination or residuals from the sacrificial carrier layers (See Method Section for more details). Furthermore, this annealing step promotes the oxygen reduction of the STO to obtain conducting membranes. The step-terrace features of the STO remain also after the transfer and the heat treatment, as shown by the AFM images (Figure 2A$_{ii}$,B$_{ii}$). The details of the fabrication and the transfer of STOm are described in the Method section of Supplementary Information. The crystal structures of the transferred STOm reveal a slight distortion with larger 001 crystal constant ($c > a$) (Figure S2, Supporting Information), which could probably be due to the relaxation of the freestanding membrane when they are released from the SAO. The ARPES experiments were performed on as-received STOm without surface treatment. To demonstrate the viability of our methodology, we have compared the electronic structures of the membranes (10 and 30 nm) with a TiO_2-terminated STO (001) single crystal substrate (with 0.5% Nb dopant) using ARPES with surface-sensitive VUV incident light.

The in-plane Fermi surfaces (FSs) of STOm and STO single crystal wafer (STOw) (Figure 2C$_i$-E$_i$) are acquired with photon

energies $h\nu = 85$ eV, and particularly probing momentum space $k_z = 6\pi$ in bulk Brillioun zone (BZ) (Figure S3, Supporting Information). The polarization of incident light (Figure 2C$_i$-E$_i$) is set to be circular polarization (*C*), which probes both the *in-plane* d_{xy} and the *out-of-plane* d_{xz}/d_{yz} orbitals. The *in-plane* FSs of the STOm (thicknesses of 10 and 30 nm) and the STOw show one circular Fermi pocket and two intersecting ellipsoidal pockets belonging to the light d_{xy} orbital and heavy d_{xz}/d_{yz} orbitals, respectively (dashed pockets in Figure 2C$_i$-E$_i$).[30–34] Figure 2C$_{ii}$-E$_{ii}$ displays the electronic structures along Γ-*X* direction measured by linear vertical (*LV*) polarization, mainly probing the d_{xy} and d_{yz} orbitals (Figure 1B). The observed "waterfall-like" intensities extending to higher binding energy (E_B) of d_{xy} bands (Figure 2C$_{ii}$-E$_{ii}$) are attributed to the polaron formation,[33,34] which originates from electron-phonon interaction (EPI) between the electrons and breathing LO_3 phonon mode in the STO lattice.[33] When comparing the STOm and STOw, the d_{xy} bands of the membranes shift to lower E_B with the band bottoms around 200 meV resulting in an energy splitting of t_{2g} bands (inset panel in Figure 2E$_{ii}$). The origin of the t_{2g} splitting is still debated in the literature, and it can be due to surface polarization,[35] electric field,[34] or tetragonal distortion.[36] The extracted value of Δt_{2g} ($= d_{xz} - d_{xy}$) for the STOm (≈180 meV) (details are shown in Figure S3, Supporting Information) is found to be much larger than the STOw (≈60 meV) (Figure 2F), which is probably due to the strain relaxation of the freestanding membranes leading to a large splitting.[37] The pure linear dispersion of STOm and STOw along k_z for d_{xy} bands show 2D character, while the d_{xz} and the d_{yz} bands exhibit 3D character (Figure S4, Supporting Information). Those findings suggest that for membrane down to thickness of 10 nm, the t_{2g} bands are still similar to the bulk material, showing a mixture of 2D and 3D characters.[32,34] However, it is crucial to highlight that the electronic response of STOm to irradiation is more akin to STO films grown on STOw (Figure S4, Supporting Information),[38] while the electronic structures are more wafer-like.[30–34]

We turn now to the study of coherent and incoherent nature of the 2D states in STOm by investigating the EPI, electron scattering, and quasiparticle lifetime, which play an important role in determining the physical properties of STO.[39] The peak-dip-hump line shape of the energy distribution curves (EDCs) at Fermi wavevector $k_F{}^{xy}$ indicates the polarons induced by the interaction between phonons and electrons (Figure 2C$_{iii}$-E$_{iii}$).[32,34] A more robust hump structure in thinner membranes signifies a stronger EPI (Figure 2C$_{iii}$-E$_{iii}$). The strength of EPI can be quantified by quasi-particle (QP) residue, Z_0, and fitted by Franck-Condon mode by considering single LO3 phonon.[32] Fitting details are shown in Supplementary Information. The fitted Z_0 of STOm and STOw reveal a continuous decrease of Z_0 for thinner membranes (Figure 2G) and increase of EPI strength when decreasing the membrane thickness. The coupling constants (α) derived from Z_0 by Monte Carlo method reveal $\alpha \approx 1.4$ for the 10 nm STOm and $\alpha \approx 1.1$ for the 30 nm STOm.[40,41] This suggests a weak coupling regime, which can be described as Fröhlich polaron,[40] a quasiparticle formed by long-range collective excitation in a periodic lattice. Furthermore, fitting the momentum distribution curves (MDCs) at Fermi level (E_F) for the STOm and the STOw by Lorentzian distribution depicts a significant increase of FWHM of the d_{xy} bands for the 10 nm STOm (Figure 2H). The imaginary part of the quasiparticle self-energy (which is equal to half the inverse lifetime in a Fermi liquid) can be obtained from the linewidths of MDCs in the ARPES spectra. Thicker membranes (>30 nm) show a comparable quasiparticle lifetime value to the STO wafer (Figure 2H). Although the possible defects and lattice distortions increase the EPI strength and decrease the quasiparticle lifetime for thinner membranes, the incoherent interactions and electron scattering indicate the comparable functioning capability of STOm with the wafer.

3. Expanding the Realm of Creating Multifunctional Oxide Systems

As discussed above, fabricating free-standing heterostructures based on STOm epitaxial on any substrate significantly expands the possibility of fundamental research and applications. Here we demonstrate the potential of depositing high-quality epitaxial complex oxides thin films on (001) $SrTiO_3$ membrane placed on Si using pulsed laser deposition. Strontium niobate, $SrNbO_3$, is an example of a correlated transparent conductor oxide[42] which has gained interest in recent years due to its large gap between the (filled) conduction and valence states, non-trivial topology,[43,44] and dimensionality-confined superconductivity.[45] Despite the significant lattice mismatch between the STO and the SNO, we show that high-quality $SrNbO_3$ thin films were successfully prepared on free-standing STOm (see more detailed in the Methods), as was confirmed by ARPES.

We fabricate $SrNbO_3$ thin films with different thicknesses of 7, 25, and 50 u.c. (3, 10, and 20 nm) on STOm integrated on Si wafer (**Figure 3**A,B). In-situ ARPES measurements were carried out after each SNO deposition (Figure 3C). All ARPES data in Figure 3 are measured at $h\nu = 106$ eV and by circular polarization. Previous theoretical studies[43,44] and recent ARPES results[46] indicate the emergent octahedral tilting in epitaxial SNO films on STO (100) single crystal substrate, inducing a band folding with non-trivial topology[43] (Figure S6, Supporting Information). The core-level spectra of SNO thin film reveal the stoichiometry of SNO film on the STOm (Figure S7, Supporting Information). The FSs of SNO with different thicknesses deposited on STOm are compared with SNO deposited directly on single crystal STO. Similar circular Fermi pockets centered at Γ point (Figure 3D$_i$,G$_i$) were observed for both SNO/STOm and SNO/STOw, which originated from the d_{xy} band of the SNO. The large square-like pockets centered at *M* point form a quasi-linear FS feature along Γ-*X* directions (Figure S6, Supporting Information) which are partially visible at an energy of $h\nu = 106$ eV (Figure 3D$_i$-G$_i$), but more clearly at $h\nu = 76$ eV (Figure S7, Supporting Information). Notably, 2D curvature maps around *M*, which highlight bands with relatively low intensities, reveal additional circular Fermi pockets centered at *M* (Figure 3D$_i$-G$_i$). These pockets originate from octahedral tilting, causing an original BZ to fold ($\sqrt{2} \times \sqrt{2}$ reconstruction), creating the M point of cubic BZ to be a new Γ of reconstructed BZ (Figure S6, Supporting Information). The presence of $a^0a^0c^+$ band reconstructions[46] induces Dirac-type band crossings protected by non-symmorphic symmetries,[43] leading to topological non-trivial states. The band dispersion along the

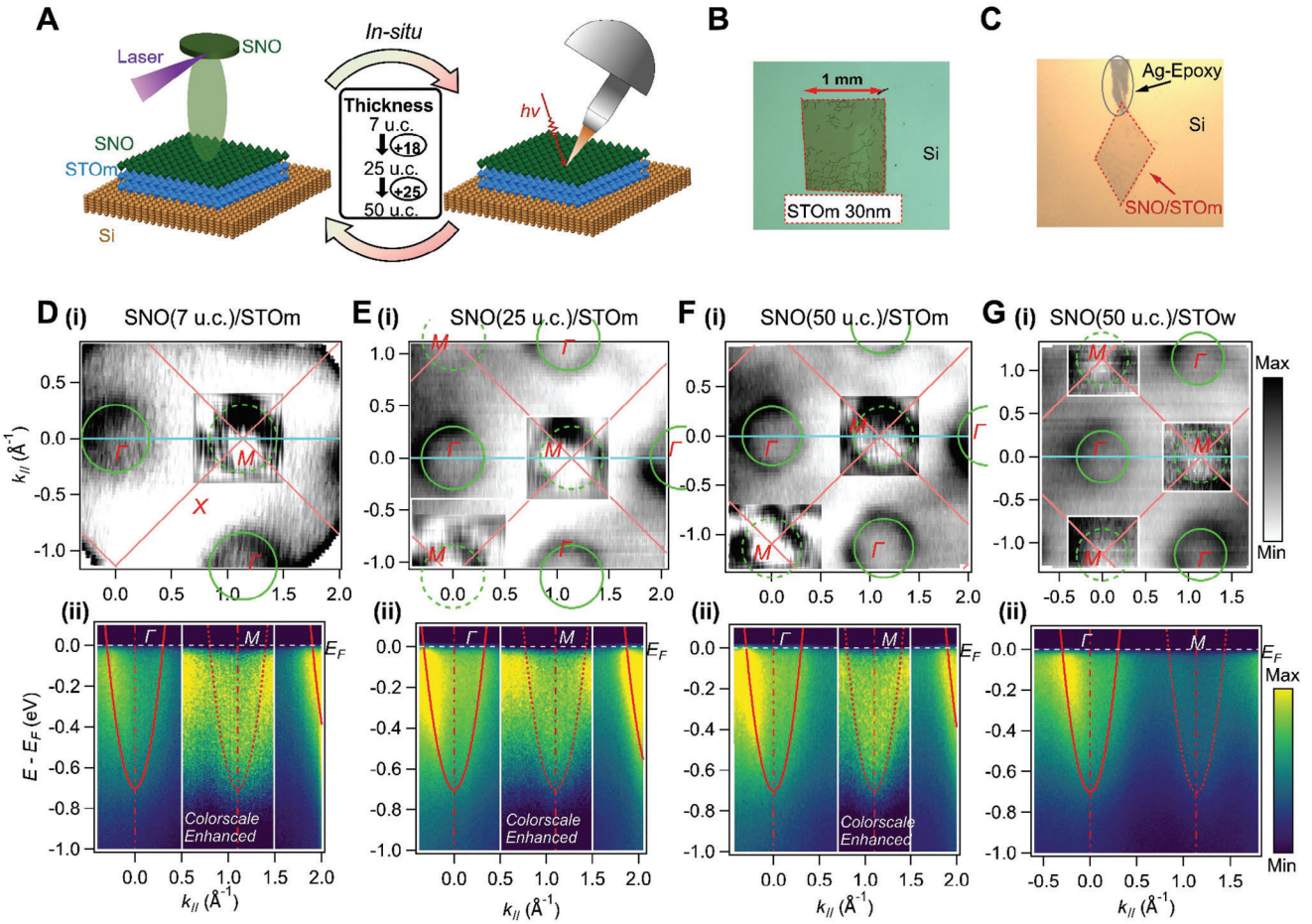

Figure 3. The electronic structures of SNO/STOm and SNO/STOw. A) Schematic of the fabrication of $SrNbO_3$ films with different thicknesses and in-situ ARPES study. B) microscopic photograph of 30 nm STOm (flake marked by red-dashed lines) after transfer. This membrane is used as the substrate to prepare SNO/STOm heterostructure. C) photograph of SNO/STOm in ARPES chamber. SNO/STOm is marked by the red dashed lines. The silver epoxy (indicated by grey circle) is used for grounding the membranes. D to G) (i), FS intensity map of SNO film grown on STOm with thicknesses of 7, 25, 50 u.c., and the referenced 50 u.c. SNO films grown on STO wafer, respectively. (ii), band dispersions along Γ-*M* direction (cyan lines in FS maps) of SNO films grown on STOm with the thicknesses of 7, 25, 50 u.c., and the referenced 50 u.c. SNO films grown on STO wafer, respectively. The light red solid lines in (i) mark the cubic BZ boundary in FS map. The green solid and dashed circles indicate the electron pocket at Γ and the folded pockets at *M* of cubic BZ, respectively. Red solid and dashed curves in the band dispersions in (ii) mark the electron band at Γ and *M*, respectively. The red dot-dashed lines mark the high symmetry points. The 2D curvature maps around *M* points are plotted on (i) to highlight the weak pockets. The color scale around *M* in (ii) is enhanced to highlight the electron bands near *M*. All ARPES data in this figure are measured at $h\nu = 106$ eV, corresponding to the $k_z = 0$ plane (Figure S7, Supporting Information).

Γ-*M* high symmetry lines shows an electron band at *M* with identical band features, which are folded d_{xy} bands by the octahedral tilting (Figure 3D$_{ii}$-G$_{ii}$). The highly dispersive nature of the bands along Γ-*M* direction indicates a small effective mass of the carriers, which we calculated to be $m^* = 0.44\ m_e$, similar to the $m^* = 0.46\ m_e$ of previous ARPES studies on SNO.[47] The correlation strength, $Z_k = m_0/m^*$ (m_0 represents the bare band mass) of SNO/STOm is $Z_k \approx 0.5$, which is higher than isostructural $SrVO_3$ or $CaVO_3$.[48] It suggests the potential of high mobility of SNO/STOm system among the transparent correlation perovskite metals. The good agreement of electronic structures of SNO films grown on STO membranes (Figure 3D-F) and wafer (Figure 3G) as well as theoretical calculations (Figure S6, Supporting Information)[44] indicates the functionality and application potential of SNO/STOm system.

Another transparent conductor, but with $3d^1$ occupation, $SrVO_3$, has been widely studied due to its good optical transmittance[48] and strong correlation nature.[49–51] We studied 7 and 20 u.c. (3 and 8 nm) of SVO thin films deposited on a 30 nm membrane of STO on Si (**Figure** 4A) and compared it with 20 u.c. of SVO deposited on TiO_2 terminated STO (100) wafer. The detailed fabrication procedures are described in the Method section. The core level spectra of the SVO/STOm and the SVO/STOw (shown in the Figure S8, Supporting Information) indicate that the stoichiometry of both SVO films is similar. Usually, SVO is crystalized in cubic structure[49–51] with the space group #221 (Figure 4C$_i$). In the cubic phase, the FS of the SVO consists of one quasi-circular electron pocket centered at the Γ point and a linear-like FS features along the k_x/k_y direction (as shown by the schematic

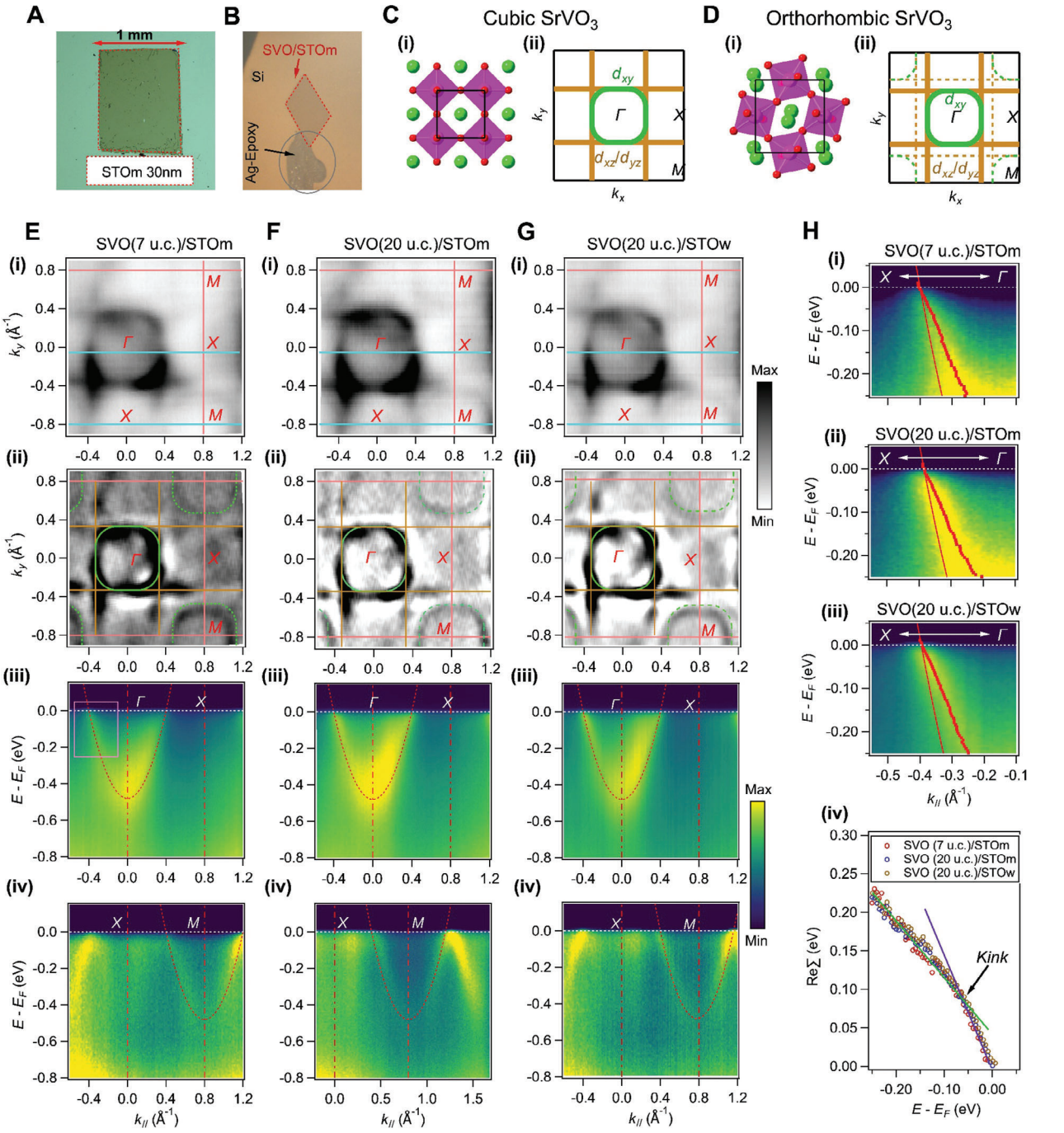

Figure 4. Electronic structures of SVO/STOm and SVO/STOw. A) Microscopic photograph of 30 nm STOm (flake marked by red-dashed lines) after transfer. This membrane is used as the substrate to prepare SVO/STOm heterostructure. B) photograph of SVO/STOm in ARPES chamber. SVO/STOm is marked by the red dashed lines. The silver epoxy (grey circle) is used for grounding the membranes. C) (i) Crystal structure of cubic SVO. Green, pink and red spheres indicate the Sr, V, and O atoms, (ii) Schematic of FS feature of cubic SVO in $k_z = 0$ plane. The green and brown pockets in (ii) mark the d_{xy} and d_{xz}/d_{yz} bands, respectively. D) same as C but for orthorhombic SVO. The dashed green and brown bands in D mark the folded electronic structures by orthorhombic distortion. E) Electronic structures of 7 u.c. SVO/STOm. (i) FS intensity map. (ii) 2D curvature of constant energy contour at $E = E_F - 0.1$ eV. (iii),(iv), ARPES intensity spectra along high symmetry lines (cyan lines in (i)) of Γ-*X* and *X*-*M*, respectively. The light red lines in (i) and (ii) mark the BZ boundary of cubic SVO. Green and brown solid FS in (ii) mark the original electronic structure of cubic SVO. Dashed green pockets in (ii) mark the folded Fermi pockets by orthorhombic distortion. Red dot-dashed lines in (iii) and (iv) mark the high symmetry points. Red dashed curves in (iii) and (iv) indicate the electron band centered at Γ and *X*, respectively. F and G) same as E but for 20 u.c. SVO/STOm and 20 u.c. SVO/STOw, respectively. H) (i-iii), zoom in electronic structures along Γ-*X* directions of E_{iii}-G_{iii}, respectively. The zoom-in range is shown in E_{iii}. The red dots represent the extracted MDC peaks and red curves indicate the bare band. (iv), The real part of self-energy Σ calculated from (i-iii) in the function of binding energy. All data in this figure is captured at $h\nu = 66$ eV and circular polarization.

in Figure 4C$_{ii}$), which belongs to the d_{xy} and d_{xz}/d_{yz} orbitals, respectively.

Interestingly, an additional circular Fermi pocket centered at *M* is identified for both SVO/STOm, and SVO /STOw films in the 2D curvature maps of constant energy contour at $E = E_F - 0.1$ eV (Figure 4E$_{ii}$-G$_{ii}$). This feature is probably due to the orthorhombic distortion. This crystal symmetry reduces the area of cubic BZ by half and folds the pockets at Γ to *M*, as illustrated in Figure 4D. In the band dispersion along the *X*-*M* direction, the electron bands around *M* (dashed curves in Figure 4E$_{iv}$-G$_{iv}$), with similar dispersion to Γ, originate from the folded d_{xy} band by the distortion of the crystal. The observations of identical electronic structure and band reconstruction for the 7 and the 20 u.c. of SVO deposited on the STOm (Figure 4E,F) suggest that the thickness plays a minor role. The strong correlations that always result in an energy kink in the real part of self-energy (ReΣ), which is detected when comparing the measured band dispersion and the bare band. The binding energy of ReΣ kink usually reflects the origin of correlations. For both SVO/STOm and SVO/STOw, the ReΣ shows a similar kink structure with binding energy E_{kink} ≈60 meV (Figure 4H), which corresponds to the electron-phonon interactions in SVO and well-studied by ARPES.[49–51] Notably, the resemblance of the electronic structure of SVO films grown on the membrane to the one deposited directly on TiO_2 terminated STO (100) single crystal indicates that STOm can serve as a high-quality substrate, like STOw. Using STOm as a flexible platform enables further tunability of SVO, which is sensitive to strain, that can enhance correlations (potentially inducing metal-insulator transition) or alter the optical properties.[48,52]

4. Transcendent Quest to a flexible High-Temperature Superconductor

The STO also serves as a universal substrate in fabricating high-temperature superconducting films, not necessarily only for perovskites. A noteworthy example is FeSe, the dichalcogenide that can be grown with high quality on STO substrates utilizing both Molecular Beam Epitaxy (MBE) methods[53] and PLD techniques.[54] Furthermore, experimental observations indicate a pronounced augmentation of superconductivity in thin film FeSe when cultivated on an STO (001) wafer.[55] Yet the mechanisms of such high-temperature superconductivity are still intensively debated. Some studies attribute it to the strong electron-phonon coupling (EPC) between the cooper pairs in FeSe layer and the phonons in STO substrate.[56–58] Moreover, it is argued that this mechanism boosts the transition temperature to over 100 K for monolayer FeSe/STO films.[56] However, the strain applied here is considered to be the key parameter to tune the phonon mode, suggesting STOm as a promising template for further modulation of superconductivity in FeSe films.

Inspiringly, we have used the STOm to fabricate FeSe superconducting films on Si. The usual etching procedure to produce TiO_2-terminated STO is not possible for the membranes. Since the superconductivity is sensitive to the surface termination of the substrate and the surfaces of the STOm probably have a mixed termination (TiO_2 and SrO, Figure S5, Supporting Information), we provided TiO_2-termination substrate in another way. We first deposited 20 u.c. anatase-TiO_2 (*a*-TiO_2) films on as-received STOm (**Figure 5B**) to acquire a "TiO_2-like" terminated substrate (details of fabrication procedure are shown in the Method Section) (Figure 5A). The quality of TiO_2 films was confirmed by performing an in-situ ARPES experiment on *a*-TiO_2/STOm and comparing these results with the same thickness of *a*-TiO_2 deposit on a single crystal TiO_2-terminated STO (100) (See Figure S9, Supporting Information). The observed one-band FS originates from the lowered d_{xy} band due to the tetragonal symmetry of *a*-TiO_2. The results reveal the absence of 4 × 1 surface reconstruction, which was observed in previous studies.[59] One possible explanation is that the flexible nature of membranes relaxes the lattice of epitaxial *a*-TiO_2 films. However, the absence of 4 × 1 reconstruction of FS causes this system to be purely 2D.

FeSe films with a thickness of 3 u.c. were deposited on *a*-TiO_2/STOm (Figure 5A) (Detailed growth procedure is shown in the Method section) and were investigated for their electronic structures using the in-situ PLD deposition coupled with the ARPES. The FSs of FeSe/*a*-TiO_2/STOm consist of a circular pocket centered at Γ and two intersected ellipse-like pockets centered at *M* (Figure 5D$_{i,ii}$), which is the typical two-domain FS feature of bulk FeSe or thick FeSe films[53,54,60–62] (Figure 5C). Former APRES studies reveal similar bulk-like electronic structures of FeSe films when the thickness is above 3 u.c..[53] The band dispersions near Γ and *M* along Γ-*M* direction (Figure 5D$_{iii,iv}$) show hole-like bands at Γ point and electron-like bands at *M* point. To illustrate this observation, we display the second derivative intensity cuts along the energy direction of the band dispersions in Figure 5D$_{iii,iv}$ and plot the guided band structures onto the intensity maps (Figure 5D$_{v,vi}$). The double hole bands near E_F around Γ (Figure 5D$_v$) and the double electron/hole bands around *M* (Figure 5D$_{vi}$) can be identified clearly. ARPES study demonstrates that the electronic structure of the FeSe on the STOm or single crystal STO substrate is identical (Figure 5D,E), indicating that the fabricated FeSe films on membrane system are fully applicable in functional superconducting films and the study of electronic structures.

It was reported that multiple parameters could control the band topology and superconductivity of FeSe: (i) Strain– either by the thickness control of FeSe film[53] or applying pressure,[63] (ii), Strong EPC between electrons in FeSe and the phonon mode in STO substrate.[56–58] Moreover, a band shift of ≈10 meV to lower binding energy of thick FeSe film (20 u.c.) deposit on STOm is detected in ARPES spectra (Figure S10, Supporting Information). This, likely rigid band shift, is probably due to the charge transfer from the conducting membrane substrate to the FeSe film.

Taking advantage of the flexible nature, the STOm can widen manipulation with strain and EPI, consequently offering a new route in the study of the mechanism of iron-based superconductivity and even realizing higher T_c in 2D FeSe films grown on the top.

5. Summary and Outlook

We present a method to cultivate heteroepitaxial membranes of exceptional quality using a $SrTiO_3$ (STO) nanomembrane template, which can be placed on any wafer. Leveraging this platform, we have used ARPES to confirm the high-quality chemical and electronic structure of diverse functional oxides, including $SrNbO_3$, $SrVO_3$, anatase TiO_2, and the high T_c

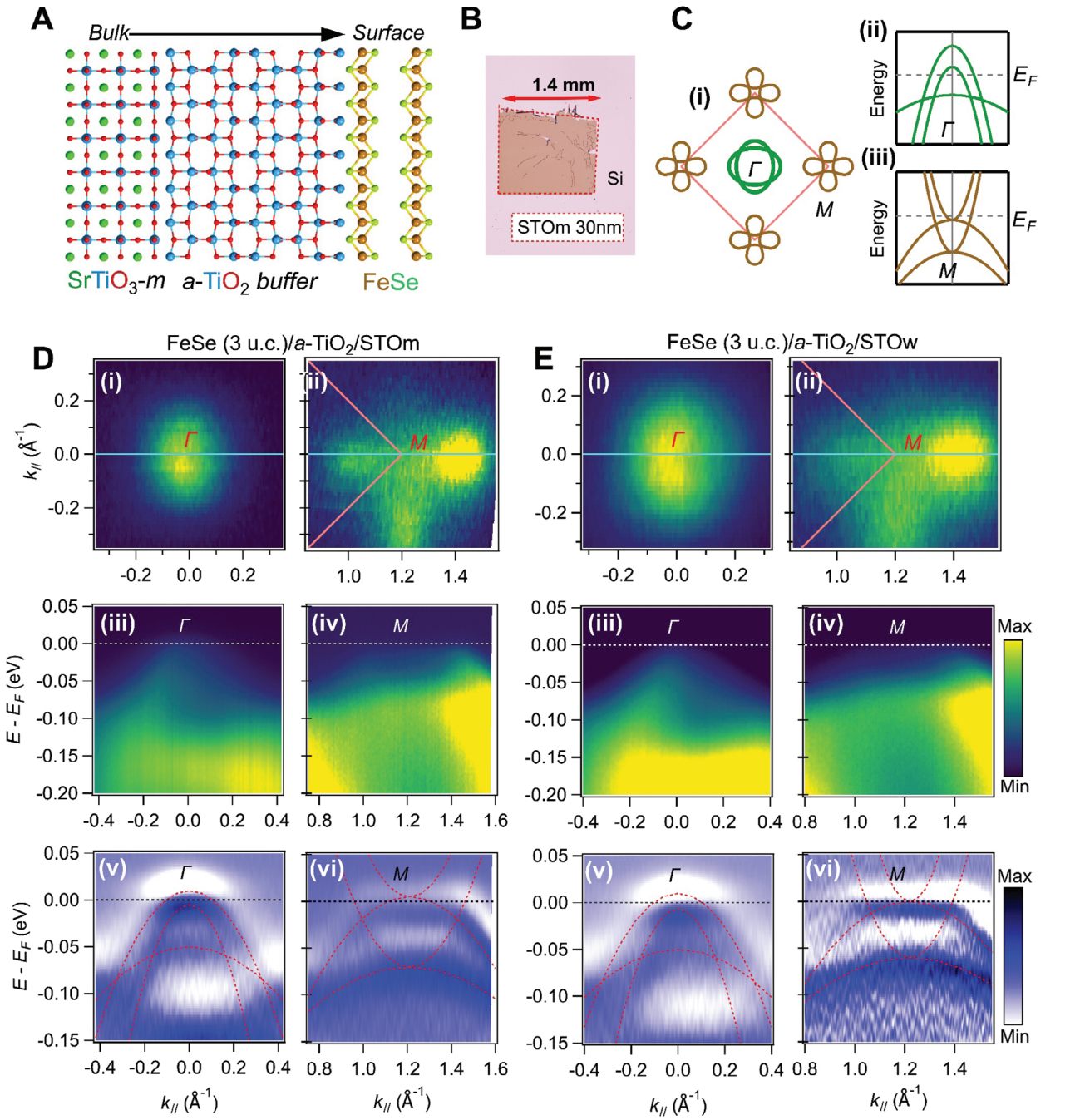

Figure 5. Electronic structure of *a*-TiO_2/STOm and FeSe/*a*-TiO_2/STOm. A) Schematic of FeSe/*a*-TiO_2/STOm heterostructure. B) microscopic photograph of as-received 30 nm STOm integrated on Si. It was used as the substrate in the study of FeSe/*a*-TiO_2/STOm. The flake marked by red-dashed lines is the membrane. There's an accidental scratch across the membranes when transferred to Si. C) typical FS features (i) and band structures (ii,iii) of bulk FeSe. The green and brown curves mark the bands near Γ and *M*, respectively. D) electronic structures of FeSe(20 u.c.)/*a*-TiO_2/STOm: (i,ii), ARPES FS maps around Γ and *M*, respectively. Light red lines mark the BZ boundary. (iii,iv), ARPES intensity cuts near Γ and *M* along Γ-*M* (cyan lines in (i) and (ii)). White dashed lines mark the E_F. Red dot-dashed lines mark the high symmetry points. (v,vi), 2nd derivative intensity cuts long energy direction of cuts in (iii) and (iv). The plotted red dashed curves guide the band structures. E) same as D but for referenced FeSe (20 u.c.)/STOw.

superconductor FeSe. The data demonstrate that films grown on STO membranes often match or even surpass the quality of those grown directly on STO single crystal (Figure S11, Supporting Information). In addition, the successful fabrication of FeSe thin films on STO membrane indicates the potential for growing $FeTe_xSe_{1-x}$, an iron-based Majorana system[64,65] with high potential for quantum computing and integrating it directly with Si technology. Overall, our research demonstrates the application of a universal technique for producing innovative film-membrane systems, capitalizing on their flexibility and

freestanding attributes for high throughput. The ability to integrate oxides into semiconducting wafers or other functioning materials opens up the opportunities for multi-dimensional manipulation of novel properties.

Supporting Information

Supporting Information is available from the Wiley Online Library or from the author.

Acknowledgements

N.P. acknowledges the support of Novo Nordisk Foundation Challenge Pro-gramme 2021: Smart nanomaterials for applications in life-science, BIOMAG Grant NNF21OC0066526, the support from the ERC Advanced "NEXUS" Grant 101054572 and the Danish Council for Independent Research Technology and Production Sciences for the DFF- Research Project 3 (grant No 00069B). A.C. acknowledges the support of the European Union's Horizon 2020 research and innovation program under the Marie Skłodowska-Curie grant agreement No 884104 (PSI-FELLOW-III-3i).

Open access funding provided by ETH-Bereich Forschungsanstalten.

Conflict of Interest

The authors declare no conflict of interest.

Author Contributions

H.L., S.Y., and A.C. contributed equally to this work. M.R. and N.P. conceived the project. S.Y. fabricated the STO membranes and performed basic characterization with the help from T.T., E.B., C.H.C., H.L., A.C., and M.R. performed the ARPES experiment with the help from N.C.P. and M.S. A.C., H.L., and M.R. fabricate thin films on the membranes by PLD. V.R. performed the DFT calculations. H. L. processed the ARPES data. H.L. wrote the manuscript with the substantial help from M.R., N.P., and useful discussions with all other authors.

Data Availability Statement

The data that support the findings of this study are available from the corresponding author upon reasonable request.

Keywords

ARPES, heteroepitaxial growth, transition metal-oxide membrane

Received: November 4, 2023
Revised: January 16, 2024
Published online:

[1] A. Ohtomo, H. Y. Hwang, *Nature* **2004**, *427*, 423.
[2] Y. Z. Chen, N. Bovet, F. Trier, D. V. Christensen, F. M. Qu, N. H. Andersen, T. Kasama, W. Zhang, R. Giraud, J. Dufouleur, T. S. Jespersen, J. R. Sun, A. Smith, J. Nygård, L. Lu, B. Büchner, B. G. Shen, S. Linderoth, N. Pryds, *Nat. Commun.* **2013**, *4*, 1371.
[3] K. Ahadi, L. Galletti, Y. Li, S. Salmani-Rezaie, W. Wu, S. Stemmer, *Sci. Adv.* **2019**, *5*, 0120.
[4] H. Lee, N. Campbell, J. Lee, T. J. Asel, T. R. Paudel, H. Zhou, J. W. Lee, B. Noesges, J. Seo, B. Park, L. J. Brillson, S. H. Oh, E. Y. Tsymbal, M. S. Rzchowski, C. B. Eom, *Nat. Mater.* **2018**, *17*, 231.
[5] P. Zubko, S. Gariglio, M. Gabay, P. Ghosez, J. M. Triscone, *Annu. Rev. Condens. Matter Phys.* **2011**, *2*, 141.
[6] J. A. Sulpizio, S. Ilani, P. Irvin, J. Levy, *Annu. Rev. Mater. Res.* **2014**, *44*, 117.
[7] Z. Huang, Ariando, X. R. W., A. Rusydi, J. Chen, H. Yang, T. Venkatesan, *Adv. Mater.* **2018**, *30*, 1802439.
[8] K. S. Novoselov, A. K. Geim, S. V. Morozov, D. Jiang, Y. Zhang, S. V. Dubonos, I. V. Grigorieva, A. A. Firsov, *Science* **2004**, *306*, 666.
[9] Y. Cao, V. Fatemi, S. Fang, K. Watanabe, T. Taniguchi, E. Kaxiras, P. Jarillo-Herrero, *Nature* **2018**, *556*, 43.
[10] D. Lu, D. J. Baek, S. S. Hong, L. F. Kourkoutis, Y. Hikita, H. Y. Hwang, *Nat. Mater.* **2016**, *15*, 1255.
[11] D. Ji, S. Cai, T. R. Paudel, H. Sun, C. Zhang, L. Han, Y. Wei, Y. Zang, M. Gu, Y. Zhang, W. Gao, H. Huyan, W. Guo, D. Wu, Z. Gu, E. Y. Tsymbal, P. Wang, Y. Nie, X. Pan, *Nature* **2019**, *570*, 87.
[12] D. Lu, S. Crossley, R. Xu, Y. Hikita, H. Y. Hwang, *Nano Lett.* **2019**, *19*, 3999.
[13] S. S. Hong, M. Gu, M. Verma, V. Harbola, B. Y. Wang, D. Lu, A. Vailionis, Y. Hikita, R. Pentcheva, J. M. Rondinelli, H. Y. Hwang, *Science* **2020**, *368*, 71.
[14] F. M. Chiabrera, S. Yun, Y. Li, R. T. Dahm, H. Zhang, C. K. R. Kirchert, D. V. Christensen, F. Trier, T. S. Jespersen, N. Pryds, *Ann. Phys. (Berlin)* **2022**, *534*, 2200084.
[15] H. S. Kum, H. Lee, S. Kim, S. Lindemann, W. Kong, K. Qiao, P. Chen, J. Irwin, J. H. Lee, S. Xie, S. Subramanian, J. Shim, S. Bae, C. Choi, L. Ranno, S. Seo, S. Lee, J. Bauer, H. Li, K. Lee, J. A. Robinson, C. A. Ross, D. G. Schlom, M. S. Rzchowski, C.-B. Eom, J. Kim, *Nature* **2020**, *578*, 75.
[16] H. Kim, C. S. Chang, S. Lee, J. Jiang, J. Jeong, M. Park, Y. Meng, J. Ji, Y. Kwon, X. Sun, W. Kong, H. S. Kum, S. Bae, K. Lee, Y. J. Hong, J. Shi, J. Kim, *Nat. Rev. Meth. Prim.* **2022**, *2*, 40.
[17] A. Sambri, M. Scuderi, A. Guarino, E. D. Gennaro, R. Erlandsen, R. T. Dahm, A. V. Bjørlig, D. V. Christensen, R. D. Capua, B. D. Ventura, U. S. di Uccio, S. Mirabella, G. Nicotra, C. Spinella, T. S. Jespersen, F. M. Granozio, *Adv. Funct. Mater.* **2020**, 1909964.
[18] Y. Li, C. Xiang, F. M. Chiabrera, S. Yun, H. Zhang, D. J. Kelly, R. T. Dahm, C. K. R. Kirchert, T. E. Le Cozannet, F. Trier, D. V. Christensen, T. J. Booth, S. B. Simonsen, S. Kadkhodazadeh, T. S. Jespersen, N. Pryds, *Adv. Mater.* **2022**, *34*, 2203187.
[19] L. Merker, US Patent No. 2684,910, **1954**.
[20] H. E. Weaver, *J. Phys. Chem. Solids* **1959**, *11*, 274.
[21] J. H. Haeni, P. Irvin, W. Chang, R. Uecker, P. Reiche, Y. L. Li, S. Choudhury, W. Tian, M. E. Hawley, B. Craigo, A. K. Tagantsev, X. Q. Pan, S. K. Streiffer, L. Q. Chen, S. W. Kirchoefer, J. Levy, D. G. Schlom, *Nature* **2004**, *430*, 758.
[22] M. P. Warusawithana, C. Cen, C. R. Sleasman, J. C. Woicik, Y. Li, L. F. Kourkoutis, J. A. Klug, H. Li, P. Ryan, L. Wang, M. Bedzyk, D. A. Muller, L. Chen, J. Levy, D. G. Schlom, *Science* **2009**, *34*, 367.
[23] D. Lee, H. Lu, Y. Gu, S.-Y. Choi, S.-D. Li, S. Ryu, T. R. Paudel, K. Song, E. Mikheev, S. Lee, S. Stemmer, D. A. Tenne, S. H. Oh, E. Y. Tsymbal, X. Wu, L.-Q. Chen, A. Gruverman, C. B. Eom, *Science* **2015**, *349*, 1314.
[24] G. Dong, S. Li, M. Yao, Z. Zhou, Y. Q. Zhang, X. Han, Z. Luo, J. Yao, B. Peng, Z. Hu, H. Huang, T. Jia, J. Li, W. Ren, Z. Ye, X. Ding, J. Sun, C. Nan, L. Chen, J. Li, M. Liu, *Science* **2019**, *366*, 475.
[25] R. Xu, J. Huang, E. S. Barnard, S. S. Hong, P. Singh, E. K. Wong, T. Jansen, V. Harbola, J. Xiao, B. Y. Wang, S. Crossley, D. Lu, S. Liu, H. Y. Hwang, *Nat. Comm.* **2020**, *11*, 3141.
[26] B. Khanbabaee, E. Mehner, C. Richter, J. Hanzig, M. Zschornak, U. Pietsch, H. Stöcker, T. Leisegang, D. C. Meyer, S. Gorfman, *Appl. Phys. Lett.* **2016**, *109*, 222901.

[27] N. Reyren, S. Thiel, A. D. Caviglia, L. Fitting Kourkoutis, G. Hammerl, C. Richter, C. W. Schneider, T. Kopp, A.-S. Rüetschi, D. Jaccard, M. Gabay, D. A. Muller, J. M. Triscone, J. Mannhart, *Science* **2007**, *317*, 1196.
[28] A. D. Caviglia, S. Gariglio, N. Reyren, D. Jaccard, T. Schneider, M. Gabay, S. Thiel, G. Hammerl, J. Mannhart, J. M. Triscone, *Nature* **2008**, *456*, 624.
[29] J. W. Reiner, A. M. Kolpak, Y. Segal, K. F. Garrity, S. Ismail-Beigi, C. H. Ahn, F. J. Walker, *Adv. Mater.* **2010**, *22*, 2919.
[30] A. F. Santander-Syro, O. Copie, T. Kondo, F. Fortuna, S. Pailhès, R. Weht, X. G. Qiu, F. Bertran, A. Nicolaou, A. Taleb-Ibrahimi, P. Le Fèvre, G. Herranz, M. Bibes, N. Reyren, Y. Apertet, P. Lecoeur, A. Barthélémy, M. J. Rozenberg, *Nature* **2011**, *469*, 189.
[31] W. Meevasana, P. D. C. King, R. H. He, S.-K. Mo, M. Hashimoto, A. Tamai, P. Songsiriritthigul, F. Baumberger, Z.-X. Shen, *Nat. Mater.* **2011**, *10*, 114.
[32] N. C. Plumb, M. Salluzzo, E. Razzoli, M. Månsson, M. Falub, J. Krempasky, C. E. Matt, J. Chang, M. Schulte, J. Braun, H. Ebert, J. Minár, B. Delley, K.-J. Zhou, T. Schmitt, M. Shi, J. Mesot, L. Patthey, M. Radović, *Phys. Rev. Lett.* **2014**, *113*, 086801.
[33] Z. Wang, S. McKeown Walker, A. Tamai, Y. Wang, Z. Ristic, F. Y. Bruno, A. de la Torre, S. Riccò, N. C. Plumb, M. Shi, P. Hlawenka, J. Sánchez-Barriga, A. Varykhalov, T. K. Kim, M. Hoesch, P. D. C. King, W. Meevasana, U. Diebold, J. Mesot, B. Moritz, T. P. Devereaux, M. Radovic, F. Baumberger, *Nat. Mater.* **2016**, *15*, 835.
[34] H. Li, W. H. Brito, E. B. Guedes, A. Chikina, R. T. Dahm, D. V. Christensen, S. Yun, F. M. Chiabrera, N. C. Plumb, M. Shi, N. Pryds, M. Radovic, *Adv. Func. Mater.* **2023**, *33*, 2210526.
[35] P. Delugas, V. Fiorentini, A. Mattoni, A. Filippetti, *Phys. Rev. B* **2015**, *91*, 115315.
[36] E. B. Guedes, S. Muff, W. H. Brito, M. Caputo, H. Li, N. C. Plumb, J. H. Dil, M. Radović, *Adv. Sci.* **2021**, *8*, 2100602.
[37] E. B. Guedes, T. W. Jensen, M. Naamneh, A. Chikina, R. T. Dahm, S. Yun, F. M. Chiabrera, N. C. Plumb, J. H. Dil, M. Shi, D. V. Christensen, W. H. Brito, N. Pryds, M. Radović, *J. Vac. Sci. Technol. A* **2022**, *40*, 013213.
[38] E. B. Guedes, S. Muff, M. Fanciulli, A. P. Weber, M. Caputo, Z. Wang, N. C. Plumb, M. Radović, J. H. Dil, *Phys. Rev. Research* **2020**, *2*, 033173.
[39] J. L. M. van Mechelen, D. van der Marel, C. Grimaldi, A. B. Kuzmenko, N. P. Armitage, N. Reyren, H. Hagemann, I. I. Mazin, *Phys. Rev. Lett.* **2008**, *100*, 226403.
[40] H. Fröhlich, H. Pelzer, S. Zienau, *Phil. Mag.* **1950**, *41*, 221.
[41] A. S. Mishchenko, N. V. Prokof'ev, A. Sakamoto, B. V. Svistunov, *Phys. Rev. B* **2000**, *62*, 6317.
[42] Y. Park, J. Roth, D. Oka, Y. Hirose, T. Hasegawa, A. Paul, A. Pogrebnyakov, V. Gopalan, T. Birol, R. Engel-Herbert, *Comm. Phys.* **2020**, *3*, 102.
[43] J. M. Ok, N. Mohanta, J. Zhang, S. Yoon, S. Okamoto, E. S. Choi, H. Zhou, M. Briggeman, P. Irvin, A. R. Lupini, Y. Y. Pai, E. Skoropata, C. Sohn, H. Li, H. Miao, B. Lawrie, W. S. Choi, G. Eres, J. Levy, H. N. Lee, *Sci. Adv.* **2021**, *7*, 9631.
[44] V. Rosendal, W. H. Brito, M. Radovic, A. Chikina, M. Brandbyge, N. Pryds, D. H. Petersen, *Phys. Rev. Materials* **2023**, *7*, 075002.
[45] H. Wei, S. Chen, Y. Zou, Y. Wang, M. Yang, Q. Zhang, L. Gu, K. Jiang, E.-J. Guo, Z. G. Cheng, *arXiv* **2022**.
[46] A. Chikina, et al., *arXiv*:2311.06072 **2023**.
[47] C. Bigi, P. Orgiani, J. Sławińska, J. Fujii, J. T. Irvine, S. Picozzi, G. Panaccione, I. Vobornik, G. Rossi, D. Payne, F. Borgatti, *Phys. Rev. Materials* **2020**, *4*, 025006.
[48] L. Zhang, Y. Zhou, L. Guo, W. Zhao, A. Barnes, H.-T. Zhang, C. Eaton, Y. Zheng, M. Brahlek, H. F. Haneef, N. J. Podraza, M. H. W. Chan, V. Gopalan, K. M. Rabe, R. Engel-Herbert, *Nat. Mater.* **2016**, *15*, 204.
[49] T. Yoshida, K. Tanaka, H. Yagi, A. Ino, H. Eisaki, A. Fujimori, Z.-X. Shen, *Phys. Rev. Lett.* **2005**, *95*, 146404.
[50] S. Aizaki, T. Yoshida, K. Yoshimatsu, M. Takizawa, M. Minohara, S. Ideta, A. Fujimori, K. Gupta, P. Mahadevan, K. Horiba, H. Kumigashira, M. Oshima, *Phys. Rev. Lett.* **2012**, *109*, 056401.
[51] M. Kobayashi, K. Yoshimatsu, E. Sakai, M. Kitamura, K. Horiba, A. Fujimori, H. Kumigashira, *Phys. Rev. Lett.* **2015**, *115*, 076801.
[52] D. E. McNally, X. Lu, J. Pelliciari, S. Beck, M. Dantz, M. Naamneh, T. Shang, M. Medarde, C. W. Schneider, V. N. Strocov, E. V. Pomjakushina, C. Ederer, M. Radovic, T. Schmitt, *npj Quantum Mater.* **2019**, *4*, 6.
[53] S. Tan, Y. Zhang, M. Xia, Z. Ye, F. Chen, X. Xie, R. Peng, D. Xu, Q. Fan, H. Xu, J. Jiang, T. Zhang, X. Lai, T. Xiang, J. Hu, B. Xie, D. Feng, *Nat. Mater.* **2013**, *12*, 634.
[54] S. K. Chaluvadi, D. Mondal, C. Bigi, D. Knez, P. Rajak, R. Ciancio, J. Fujii, G. Panaccione, I. Vobornik, G. Rossi, P. Orgiani, *J. Phys. Mater.* **2021**, *4*, 032001.
[55] Q. Wang, Z. Li, W. Zhang, Z. Zhang, J. Zhang, W. Li, H. Ding, B. Ou, P. Deng, K. Chang, *Chinese Phys. Lett.* **2012**, *29*, 037402.
[56] J. Ge, Z. Liu, C. Liu, C. Gao, D. Qian, Q. Xue, Y. Liu, J. Jia, *Nat. Mater.* **2015**, *14*, 285.
[57] C. Zhang, Z. Liu, Z. Chen, Y. Xie, R. He, S. Tang, J. He, W. Li, T. Jia, S. N. Rebec, E. Y. Ma, H. Yan, M. Hashimoto, D. Lu, S.-K. Mo, Y. Hikita, R. G. Moore, H. Y. Hwang, D. Lee, Z. Shen, *Nat. Comm.* **2017**, *8*, 14468.
[58] H. Zhang, D. Zhang, X. Lu, C. Liu, G. Zhou, X. Ma, L. Wang, P. Jiang, Q. Xue, X. Bao, *Nat. Comm.* **2017**, *8*, 214.
[59] Z. Wang, Z. Zhong, S. McKeown Walker, Z. Ristic, J.-Z. Ma, F. Y. Bruno, S. Riccò, G. Sangiovanni, G. Eres, N. C. Plumb, L. Patthey, M. Shi, J. Mesot, F. Baumberger, M. Radovic, *Nano Lett.* **2017**, *17*, 2561.
[60] M. D. Watson, T. K. Kim, A. A. Haghighirad, N. R. Davies, A. McCollam, A. Narayanan, S. F. Blake, Y. L. Chen, S. Ghannadzadeh, A. J. Schofield, M. Hoesch, C. Meingast, T. Wolf, A. I. Coldea, *Phys. Rev. B* **2015**, *91*, 155106.
[61] M. D. Watson, T. K. Kim, L. C. Rhodes, M. Eschrig, M. Hoesch, A. A. Haghighirad, A. I. Coldea, *Phys. Rev. B* **2016**, *94*, 201107(R).
[62] D. Huang, J. E. Hoffman, *Annu. Rev. Condens. Matter Phys.* **2017**, *8*, 311.
[63] S. Medvedev, T. M. McQueen, I. A. Troyan, T. Palasyuk, M. I. Eremets, R. J. Cava, S. Naghavi, F. Casper, V. Ksenofontov, G. Wortmann, C. Felser, *Nat. Mater.* **2009**, *8*, 630.
[64] P. Zhang, K. Yaji, T. Hashimoto, Y. Ota, T. Kondo, K. Okazaki, Z. Wang, J. Wen, G. D. Gu, H. Ding, S. Shin, *Science* **2018**, *360*, 182.
[65] D. Wang, L. Kong, P. Fan, H. Chen, S. Zhu, W. Liu, L. Cao, Y. Sun, S. Du, J. Schneeloch, R. Zhong, G. Gu, L. Fu, H. Ding, H. J. Gao, *Science* **2018**, *362*, 333.